Quantitative Analysis of Pathological Mitochondrial Morphology in Neuronal Cells in Confocal Laser Scanning Microscopy Images

Herbert Süße[1], Wolfgang Ortmann[1], Janin Lautenschläger[2], Christian Lautenschläger[2], Marco Körner[1], Julian Grosskreutz[2], and Joachim Denzler[1]

[1] Computer Vision Group, Friedrich Schiller University of Jena
Ernst-Abbe-Platz 2, 07743 Jena, Germany
{herbert.suesse,wolfgang.ortmann,marco.koerner,joachim.denzler}@uni-jena.de
http://www.inf-cv.uni-jena.de
[2] Hans Berger Department of Neurology, Jena University Hospital
Erlanger Allee 101, 07747 Jena, Germany
{janin.lautenschlaeger,christian.lautenschlaeger,
julian.grosskreutz}@med.uni-jena.de
http://www.neuro.uniklinikum-jena.de

Abstract. The quantitative analysis of mitochondria morphology is of great interest on medical research of neurodegnerative diseases, and also for cancer disease, and *Diabetis melitus*. The state-of-the-art in mitochondrial analysis is based on length measurements of randomly selected individual mitochondria. As manual segmentation and evaluation for whole cell analysis is very time-consuming and error-prone, we present a framework for semi-automatic processing of these data which only requires a minimal amount of simple manual user interactions. The mitochondrial structures are segmented by *Oriented Differences of Boxes (ODoB)* filters and normalized to the cell volume. Thus, the core ingredient of our system is an algorithm for approximating convex hulls of point sets, called the *Regularized Geometric Hull (RGH)*. As the proposed framework produces promising results in experiments performed in cultured primary motor neurons which were successfully approved by medical experts, it will be subject to further investigation in clinical studies.

Keywords: CLSM, Neural Cells, Mitochondria, Segmentation, Convex Hull, Differences of Boxes

1 Introduction

Mitochondria are sub-cellular organelles that have the important function to provide energy production for the cell. Furthermore, they contribute to intracellular calcium handling, free-radical scavenging and induction of apoptosis. The architecture of mitochondria was revealed in the 1950s by electron microscopy studies and in the 1980s live cell microscopy studies showed that mitochondria are highly dynamic organelles that are organized as large interconnected networks with dynamic fusion and division processes[10] (*cf.* Fig. 1).
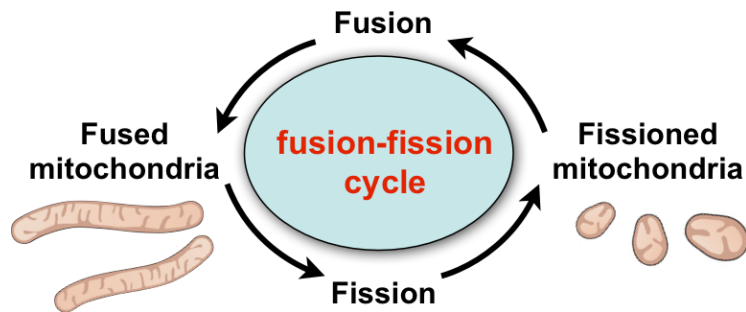
Fig. 1. According to their state within the fusion-fission cycle, mitochondria appear either line-shaped or fragmented. In pathological conditions, mitochondria remain longer in the fissioned stage or show other types of variations, which can be observed by image processing.

The lengths of mitochondria and the degree to which they form closed networks are determined by the balance between fission and fusion rates. This fine-tuned balance is influenced by metabolic but also pathologic conditions in mitochondria and their cellular environment. Fission and fusion processes are important for the maintenance of healthy mitochondria as mitochondrial DNA and metabolites can be exchanged. Thus, changes in mitochondrial morphology and distribution indicate mitochondrial dysfunction and probably an early stage in pathogenesis[1].

Alterations in mitochondrial size and shape and also metabolic dysfunctions of mitochondria are found in neurodegenerative diseases[2, 4, 5, 10] as well as *Diabetes mellitus* and cancer. Additionally, mitochondrial fission and fusion play prominent roles in disease-related processes such as apoptosis and mitophagy. The quantitative analysis of mitochondrial fragmentation in whole cells is difficult and very error-prone due to a high density of mitochondria in the cell body—as can be seen by the example given in Fig. 2(a)—but nevertheless would provide the basis for an evidence-based description of mitochondrial dysfunction as well as for the evaluation of mitochondrial therapeutic interventions. Therefore, we developed a novel computer vision algorithm for a quantitative analysis of mitochondrial fragmentation in *Confocal Laser Scanning Microscopy (CLSM)* employing *Oriented Differences of Boxes (ODoB)* filtering and *Regularized Geometric Hulls (RGH)*. The algorithm allows for the semi-automatic analysis of mitochondrial fragments in whole cell z stacks, thus avoiding random sampling of single mitochondria and gaining maximal objective results due to minimal user interaction.

The remainder of this paper is structured as follows: in Sect. 2.1 we present preprocessing steps dedicated to the segmentation of mitochondria in terms of line structures. Subsequently, Sect. 2.2 gives a theoretical introduction in the concept of *Regularized Geometric Hulls (RGH)* and shows how this tool is used in the context of cell analysis. In Sect. 3, we present our final framework and results of experimental studies in primary motoneurons. Sect. 4 summarizes and concludes this paper.
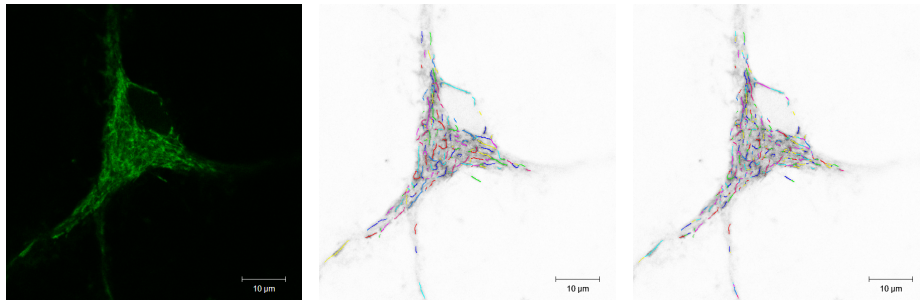
(a) neural cell with fluorescent labeled mitochondria

(b) mitochondria detected as fused lines

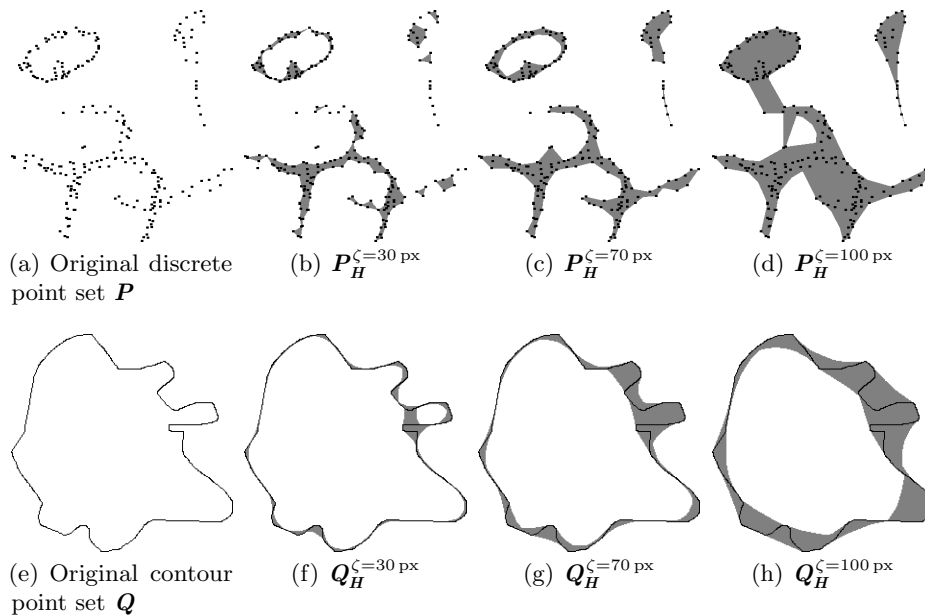(c) mitochondria after fragmentation detection

Fig. 2. The main objective of our system is to segment line structures which are considered to be fused mitochondria from individual CLSM images and quantify their degree of fractionation, which serves as an indicator for pathological conditions.

2   Image Processing

2.1   Mitochondria Segmentation

As can be seen in Fig. 2(a), CLSM images show a high density of mitochondria as well as pixel noise, which handicaps the automatic segmentation of mitochondrial structures. In order to overcome this problem, we take advantage of the *Oriented Differences of Boxes (ODoB)* operator recently presented for segmenting blood vessels in *Confocal Laser Endomicroscopy (CLE)* images[9]. This class of filters is a gradient orientation-specific extension of the classical Differences of Boxes (DoB) operator[8] and allows to smooth line structures while simultaneously suppressing noise in non-line areas, which can be used to emphasize target structure in these kind of images. In contrast to the setup used in the original work, where different filters were designed to be sensitive to various blood vessel diameters, we solely employ one single filter type, as the mitochondria are assumed to be of uniform width. For the aim of segmenting mitochondrial structures, we use local maxima of precomputed ODoB outputs to start instances of *Seeded Region Growing (SRG)*, which will result in a binary segmentation map distinguishing between hypothetical mitochondria pixels and the background. This completely unrelated set of foreground pixels is used to create a morphological skeleton, wherefrom in turn a forest of *Minimum Spanning Twhererees (MST)* is extracted in order to augment the initial set of unrelated foreground points with a neighborhood relation. In order to overcome the problem of over-segmentation, small artifacts are eliminated by applying a *Split-and-Merge (SAM)* strategy.

One major observation for pathological cases is the amount of mitochondrial fragmentation within the cell body. In order to locate fragmentation positions along the mitochondria center line, we employ a sliding window approach traversing the segmented path. For each position, we decide for local minima by applying a Top-Hat filter, which produces evident outputs at extrema positions.

(a) Original discrete point set $\boldsymbol{P}$ (b) $\boldsymbol{P}_H^{\zeta=30\,\mathrm{px}}$ (c) $\boldsymbol{P}_H^{\zeta=70\,\mathrm{px}}$ (d) $\boldsymbol{P}_H^{\zeta=100\,\mathrm{px}}$

(e) Original contour point set $\boldsymbol{Q}$ (f) $\boldsymbol{Q}_H^{\zeta=30\,\mathrm{px}}$ (g) $\boldsymbol{Q}_H^{\zeta=70\,\mathrm{px}}$ (h) $\boldsymbol{Q}_H^{\zeta=100\,\mathrm{px}}$

Fig. 3. Influence of different values for the regularization parameter ζ on geometric hull construction for the case of (a)–(d) dense point sets and (e)–(h) contour point sets. Note that the RGH preserves inner contours.

2.2 Regularized Geometric Hull

In order to put the number of mitochondria found within the cell into perspective, we need to determine the volume of the complete cell which is integrated over the areas of each z stack slice. For this purpose, we employ a new strategy for construction of geometric hulls, which we call the *Regularized Geometric Hull (RGH)*.

Definition 1 (Convex hull).
     Given an arbitrary set of Euclidean points $\boldsymbol{P} = \{\boldsymbol{p}|\boldsymbol{p} \in \mathbb{R}^2\}$ (or discrete lattice points $\boldsymbol{Q} = \{\boldsymbol{q}|\boldsymbol{q} \in \mathbb{Z}^2\}$), the Convex Hull $\boldsymbol{P}_H \supseteq \boldsymbol{P}$ ($\boldsymbol{Q}_H \supseteq \boldsymbol{Q}$) *is the smallest convex subset of $\mathbb{R}^2$ that contains $\boldsymbol{P}$ ($\boldsymbol{Q}$).*

Various algorithms for the computation of the convex hull with fair runtime complexity $\mathcal{O}(n \log n)$ exist in the field of computational geometry. As this convex hull approximation of points is insufficiently coarse for most computer vision problems, we aim to allow a certain degree of non-convexity, *i.e.* concavity, while computing geometric hulls.

Definition 2 (adjacent points).
     Let $d : \boldsymbol{M}^2 \mapsto \mathbb{R}$ be a metric in $\boldsymbol{M}^2$. Two points $\boldsymbol{p}, \boldsymbol{q} \in \boldsymbol{M}^2$ are called

adjacent *wrt. to a constant* $0 \leq \zeta \in \mathbb{R}$, *if*

$$\boldsymbol{p} \sim^\zeta \boldsymbol{q} \Leftrightarrow d(\boldsymbol{p}, \boldsymbol{q}) \leq \zeta \quad . \tag{1}$$

Definition 3 (Regularized Geometric Hull (RGH) for Euclidean point sets)**.**
Let $\boldsymbol{P} = \{\boldsymbol{p} | \boldsymbol{p} \in \mathbb{R}^2\}$ *be an arbitrary set of Euclidean points and* $\Delta(p_1, p_2, p_3) \subseteq$
$\boldsymbol{P}$ *the set of all points* $p_i \in \boldsymbol{P}$ *enclosed by the triangle defined by the 3-tuple*
$(p_1, p_2, p_3) \in \boldsymbol{P}^3$. *Let further be*

$$\boldsymbol{P}_\Delta^\zeta = \left\{ \Delta(p_1, p_2, p_3) \in \boldsymbol{P}^3 \mid p_1 \sim^\zeta p_2 \wedge p_2 \sim^\zeta p_3 \wedge p_1 \sim^\zeta p_3 \right\} \tag{2}$$

the set of all triangles of adjacent points in $\boldsymbol{P}$ *wrt. a given constant* $0 \leq \zeta \in \mathbb{R}$.
Then, the set

$$\boldsymbol{P}_H^\zeta = \bigcup \boldsymbol{P}_\Delta^\zeta \cup \boldsymbol{P} \tag{3}$$

is called the Regularized Geometric Hull (RGH) *of* $\boldsymbol{P}$ *wrt. to* ζ.

Definition 4 (Regularized Geometric Hull (RGH) for discrete lattice point sets)**.**

Let $\boldsymbol{Q} = \{\boldsymbol{q} | \boldsymbol{q} \in \mathbb{Z}^2\}$ *be an arbitrary set of discrete lattice points. Let further*
$\Delta(q_1, q_2, q_3) \subseteq \boldsymbol{Q}$ *be the set of all triangular points* $q_i \in \boldsymbol{Q}$ *induced by the*
lattice points $(q_1, q_2, q_3) \in \boldsymbol{Q}^3$ *and*

$$\boldsymbol{Q}_\Delta^\zeta = \left\{ \Delta(q_1, q_2, q_3) \in \boldsymbol{Q}^3 \mid q_1 \sim^\zeta q_2 \wedge q_2 \sim^\zeta q_3 \wedge q_1 \sim^\zeta q_3 \right\} \tag{4}$$

the set of all non-degenerated *triangles of adjacent points in* $\boldsymbol{Q}$ *wrt. a given*
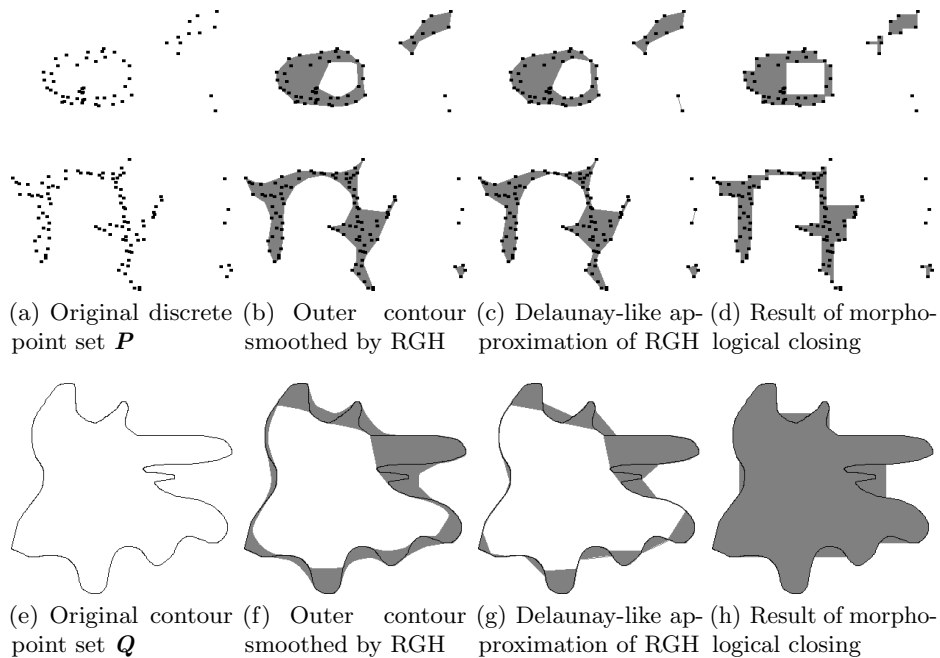*constant* $0 \leq \zeta \in \mathbb{R}$.
Then, the set

$$\boldsymbol{Q}_H^\zeta = \bigcup \boldsymbol{Q}_\Delta^\zeta \cup \boldsymbol{Q} \tag{5}$$

is called the Regularized Geometric Hull (RGH) *of* $\boldsymbol{Q}$ *wrt. to* ζ.

Apparently, the properties of the geometric hull $\boldsymbol{P}_H^\zeta$ strictly depend on the
choice of the structure parameter ζ, as can be seen in Fig. 3. If $\zeta = 0$, the geometric
hull $\boldsymbol{P}_H^0$ is identical to the point set $\boldsymbol{P}$. In turn, if $\zeta \to \infty$, the geometric hull
$\boldsymbol{P}_H^\zeta$ converges to the convex hull $\boldsymbol{P}_H$. Hence, the relation

$$\boldsymbol{P} = \boldsymbol{P}_H^0 \subseteq \boldsymbol{P}_H^\zeta \subseteq \boldsymbol{P}_H^\infty = \boldsymbol{P}_H, \quad 0 \leq \zeta \in \mathbb{R} \tag{6}$$
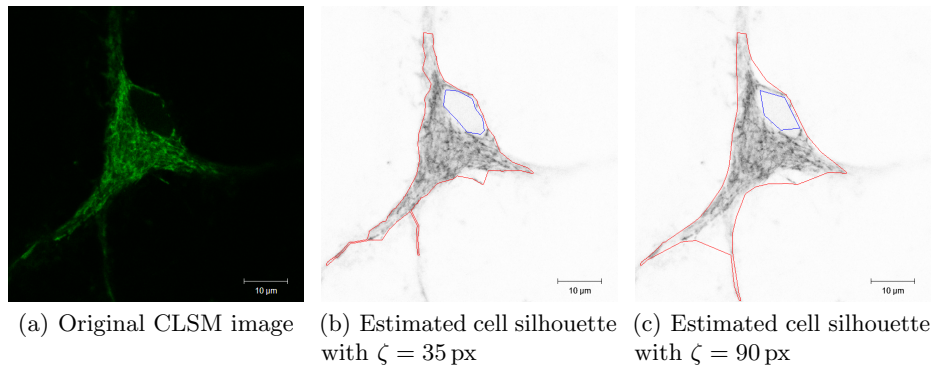
holds and it can be seen that the structure parameter ζ regularizes the convexity
or concavity of the geometric hull. In contrast to the classical convex hull $\boldsymbol{P}_H$,
the RGH $\boldsymbol{P}_H^\zeta$ describes the geometric structure of the input data $\boldsymbol{P}$ by a set of
outer and inner contours.

(a) Original discrete point set P (b) Outer contour smoothed by RGH (c) Delaunay-like approximation of RGH (d) Result of morphological closing

(e) Original contour point set Q (f) Outer contour smoothed by RGH (g) Delaunay-like approximation of RGH (h) Result of morphological closing

Fig. 4. The *Regularized Geometric Hull* can be approximated by using Delaunay-like triangulations of the input point cloud P or contour Q, which realizes a morphological closing operation with adaptive, polygonial structure elements.

Approximation As can be seen from the definitions 3 and 4, the computation of the RGH shows cubic complexity $\mathcal{O}(n^3)$ in the number n of input points which makes its application unhandy in realistic scenarios. For this reason, we approximate the underlying set of triangles $P_\Delta^\zeta \subseteq P^3$ by a modification of the *Delaunay triangulation*[3] $\widetilde{P}_\Delta^{\zeta_{\mathrm{DT}}} \subseteq P^3$, which is supposed to be a triangular tessellation of a given point set P optimal wrt. a given distance criterion. All triangles obtained by Delaunay's triangulation algorithm are drawn into a binary image, wherefrom final contours are extracted afterwards. Hence, the Delaunay triangulation $\widetilde{P}_\Delta^{\zeta_{\mathrm{DT}}}$—limited to triangles with edge lengths smaller than $0 \leq \zeta_{\mathrm{DT}} \in \mathbb{R}$—can be interpreted as an approximation of the previously used set of triangles of adjacent points P_Δ^ζ. The images shown in Fig. 4(c) and 4(g) show the results of our RGH algorithm using the Delaunay-like approximation for both a discrete point set and a set of discrete contour points, respectively. Compared to the results of the original RGH algorithm shown in Fig. 4(b) and 4(f), the results are reasonably good and useful for further processing.

As the Delaunay algorithm shows solely quasi-logarithmic complexity $\mathcal{O}(n \cdot \log n)$ in the number n of vertices, this approximation severely speeds up the whole computation and allows for real-time performance.

(a) Original CLSM image (b) Estimated cell silhouette (c) Estimated cell silhouette
with $\zeta = 35\,\mathrm{px}$ with $\zeta = 90\,\mathrm{px}$

Fig. 5. From a typical z stack slice of a neural cell as input, our algorithm can determine the boundaries of the cell body (red) and the nucleus (blue) based on the RGH computation performed on the segmented structure (*cf.* Fig. 2(c)).

Geometric Interpretation When analyzing the results of the RGH or their approximation based on Delaunay triangulation, one can observe various handy properties, which can be useful for further processing of precomputed contours or point sets. First, the RGH augments the contour or dense point set $\boldsymbol{P}$ by a *geometric orientation*, which allows to apply neighborhood-based methods for shape recognition. While doing so, in the case of discrete point sets and dependent from the structure parameter ζ, existing holes are preserved, as can be seen in Fig. 4(b) and 4(c).

Second and as illustrated in Fig. 4, the presented method performs a *smoothing* of a given contour which can be used to deal with inaccurate segmentation. Again, the impact of this smoothing is tuned by the structure parameter ζ. In terms of computational geometry, this is comparable to the *morphological closing* operator applied to binary objects. So, our method can be characterized as such a closing operation based on adaptive, polygonial structure elements. In contrast to classical morphological closing with constant regular structure elements (*e.g.* rectangles, ellipses), the results of our proposed method applied to contour and dense point sets appear much more smooth an intuitive compared to morphological closing results, as can be seen in Fig. 4(d) and 4(h), respectively.

Application for cell boundary estimation After presenting the theoretical foundations, we now show how the concept of *Regularized Geometric Hulls* can be applied for segmentation of cell bodies. As described in Sect. 2.1, we have access to an accurate segmentation of line structures within the cell, which are considered to be fused mitochondria. As mitochondrial structures are equally distributed among the cell body, we use the previously obtained segmentation as an input for RGH computation in order to estimate the actual cell body contour as well as the nucleus. Fig. 5 shows that the outer contour encloses the whole cell body, while the smoothness depends on the choice of the structure

Table 1. Statistis computed from the segmented and integrated z stack slices.

Parameter	Symbol
number of mitochondria fragments	n
mean mitochondria fragment length	μ_{mito}
mitochondria fragment length stddev.	σ_{mito}
fractal dimension	D
lacunarity	Λ
cell body area	A_{cell}
nucleus area	A_{nucleus}
effective 2D mitochondria density	$\rho_{\mathrm{2D}} = \frac{n}{A_{\mathrm{cell}} - A_{\mathrm{nucleus}}}$
cell body volume	$V_{\mathrm{cell}} = h_z \cdot \sum A_{\mathrm{cell}}$
nucleus volume	$V_{\mathrm{nucleus}} = h_z \cdot \sum A_{\mathrm{nucleus}}$
effective 3D mitochondria density	$\rho_{\mathrm{3D}} = \frac{\sum n}{V_{\mathrm{cell}} - V_{\mathrm{nucleus}}}$

parameter ζ. Furthermore, as the RGH algorithm is able to deal with nested contours (*i.e.* holes), the cell nucleus is clearly segmented. Thus, the anatomy of the cell can be analyzed automatically, which speeds up the whole procedure remarkably.

2.3 Volumetric Integration and Statistical Evaluation

While the methods presented before are designed to work on 2d images extracted from CLSM z stacks, their results have to be transformed to a volumetric representation. For this purpose, we use the results from each particular z stack slice and integrate them into a volumetric model using the metric metadata delivered by the image acquisition process. Finally, various statistical parameters are computed using the precomputed results, as outlined in Tab. 1.

3 Evaluationn in primary motoneurones

3.1 Algorithm setup

For testing and evaluation of the proposed method, we compiled the individual steps into a semi-automatic framework as outlined in Fig. 6. Initially and after visual inspection, the user has to select one slice from the z stack. This image is passed to the *ODoB* filtering module (*cf.* Subsect. 2.1) in order to suppress noise and emphasize the local mitochondrial structures. Its output is converted to a binary foreground segmentation by the *Seeded Region Growing (SRG)* module. Here, the user is able to adjust the amount of segmented mitochondria structure. After confirmation, the set of identified mitochondria pixels is converted into a *morphological skeleton* and further augmented by a neighborhood structure by the *Minimum Spanning Tree (MST)* module. Subsequently, the *Split-and-Merge* module removes virtual branches and simplifies the forest of line structure trees. In order to detect fractionation along the mitochondria center lines, the *Top-Hat* module (*cf.* Subsect. 2.1) analyzes the set of mitochondria for local minima. Again,
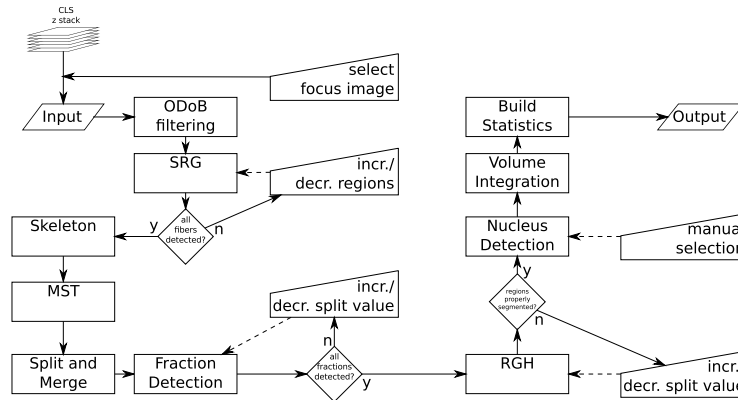
Fig. 6. The outline of our framework: dashed and solid lines attached to trapezoids indicate optional and mandatory user interaction, respectively.

the user is enabled to adjust the parameter of allowed fragmentation in order to adjust the quality. Having this set of line structures, the *Regularized Geometric Hull (RGH)* module (*cf.* Subsect. 2.2) computes optimal surrounding contours for both the boundaries of the cell body as well as the nucleus. The structure parameter ζ can be controlled by the user. After completing this procedure for the first user-selected z stack slice, the parameters used for the particular modules are stored and reused for processing the other slices. Hence, no further user interaction is necessary. Finally, all results are compiled and integrated into a volumetric representation and the statistics mentioned in Sect. 2.3 are computed.

3.2 Material and Methods

In order to perform tests on real-world data, we ran experiments using the subsequently presented parameters.

Motor neuron-enriched cell cultures Motor neuron-enriched cultures were prepared as described by Lautenschläger *et al.*[6]. Briefly, ventral spinal cords were dissected from 13-day old mouse embryos (C57BL/6J), digested for 15 min in 0.1 % trypsin (Gibco, UK) and triturated with fire polished pipettes. Motor neurons and glial cells were separated by centrifugation on a 6.2% OptiPrep cushion (Axis-shield Poc AS, Norway). Glial feeder layers were plated on poly-l-ornithin (1 mg/mL in borate buffer) coated 12 mm dishes (Marienfeld GmbH & Co. KG, Germany) at a density of 50,000 cells/dish in DMEM/Ham's F12-medium (PAA, Austria) containing penicillin (10 U/mL)/streptomycin (10 µg/mL, Gibco, UK) and fetal calf serum (10%, Lonza, Germany) for the first week, later on horse serum (10%, Gibco, UK). On reaching confluency, cell division was halted by 5 µM arabinofuranosyl cytidine (Calbiochem, Germany) for 24 h. The motor neuron enriched fraction was seeded on pre-established glial feeder layers at a
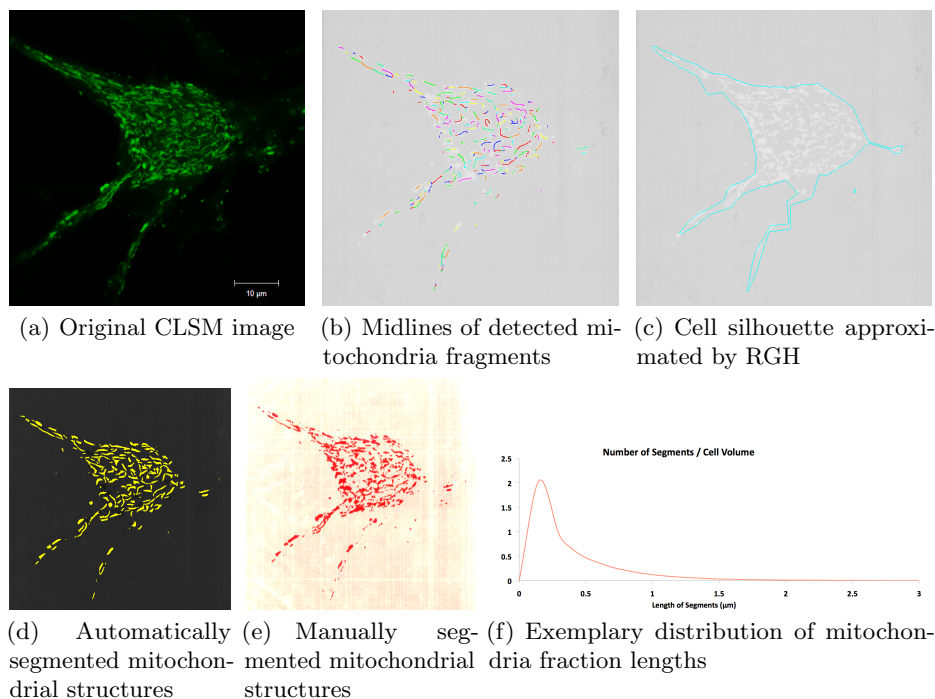
density of $30,000$ cells/dish. Motor neuron culture medium consisted of neurobasal medium (Gibco, UK), B27 neuromix (2%; Gibco, UK), N2 supplement (0.2%; Gibco, UK), l-glutamine (1 mM; Gibco, UK), horse serum (2%; Gibco, UK), penicillin (10 U/mL)/streptomycin (10 µg/mL) (Gibco, UK) and BDNF (2 ng/mL; PeproTec, Germany). The cultures were kept in a 5% CO_2-humidified incubator at $37\,°C$ and used for experiments starting on day 13 in vitro.

Mitochondrial staining To monitor mitochondrial network, the genetically targeted fluorescent indicator 4mtD3 (Ex 420 nm/Em 525 nm) was used. This indicator is a designed protein specifically targeted to mitochondria by containing 4 copies of the cytochrome C signal sequence, which makes a high localization efficiency without any disturbances of mitochondria possible. Furthermore, 4mtD3 gives the opportunity to measure Ca^{2+} concentration in mitochondria by fluorescence resonance energy transfer[7]. Motor neuron-enriched cultures were transfected with the 4mtD3 plasmid DNA using Lipofectamine 2000 (Invitrogen, UK). The standard protocol with a DNA-*vs.*-Lipofectamine 2000 ratio of 1:2 was used. Forty-eight hours after transfection, motor neuron-enriched cultures were fixed with 4% paraformaldehyde diluted in phosphate buffered saline (PBS, pH 7.4) for 20 min. Motor neurons were stained by SMI32 antibody (Covance, CA, USA) and the secondary antibody Alexa 594 goat anti mouse (Invitrogene, UK; Ex 590 nm/Em 617 nm). Finally DAPI (Ex 345 nm/Em 455 nm) was applied to stain nuclei and coverslips were embedded in Fluoromount-G™.

Mitochondrial visualization The stained motor neuron-enriched cultures were examined by a ZEISS LSM 710 *Confocal Laser Scanning Microscope (CLSM)*. Motor neurons were identified by SMI32 staining and captured as *z* stacks (200 nm distance between stack layers) using a 63X oil immersion objective. Pinhole was set 0.25 to minimize off slice light enabling a clear visualization of mitochondrial structures.

3.3 Evaluation

As we are not aware of any standard procedure to compare manual and automatic segmentation of mitochondria, we present a collection of qualitative examples. In Fig. 7, some results are shown and compared to a manual segmentation performed by an expert. It can be seen that the segmentation results obtained by our proposed method approximate the expert segmentation in a reasonable good way. This observation was approved by several medical experts. As mentioned before, the segmentation of mitochondria is used for computing statistical parameters in order to quantify the degree of fragmentation. One very important feature is the distribution of mitochondria segment lengths, which is exemplary shown in Fig. 7(f). To date, mitochondria analysis is based on manual length measurements of randomly selected individual mitochondria, which is very time-consuming and error-prone. In contrast, our approach operates instantly and so speeds up the whole diagnostic pipeline in a remarkable extend.

(a) Original CLSM image

(b) Midlines of detected mitochondria fragments

(c) Cell silhouette approximated by RGH

(d) Automatically segmented mitochondrial structures

(e) Manually segmented mitochondrial structures

(f) Exemplary distribution of mitochondria fraction lengths

Fig. 7. Top row: the individual stages of our framework; bottom row: comparison between manual and automatic segmentation and derived fraction length statistics.

4   Summary

We presented a novel framework for the automatic segmentation and structural analysis of mitochondria degeneration in neural cells, which is regarded as a stable indicator for pathological conditions. For this purpose, we introduced *Regularized Geometric Hulls (RGH)* for estimating enclosing contours of given point sets which allows to control the properties of the obtained geometric hull by tuning one single parameter in order to regularize the convexity of the obtained hull. While the results of our framework were proven to be comparable or superior to manual human expert annotations, we can reduce the amount of user interaction to a minimal amount, which speeds up the whole procedure remarkably.

References

1. van der Bliek, A.M., Shen, Q., Kawajiri, S.: Mechanisms of mitochondrial fission and fusion. Cold Spring Harbor perspectives in biology 5(6), 1–16 (2013)
2. Chan, D.C.: Mitochondria: dynamic organelles in disease, aging, and development. Cell 125(7), 1241–1252 (2006)
3. Delaunay, B.: Sur la sphère vide. USSR Academy of Sciences (6), 793–800 (1934)
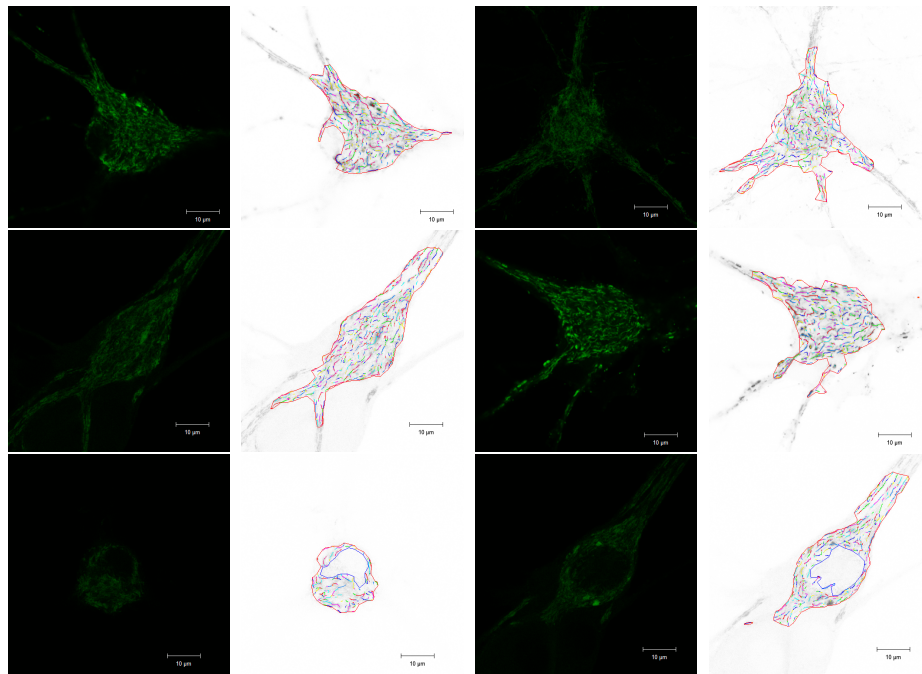
Fig. 8. Example results of our proposed mitochondria detection method.

4. Edwards, J., Quattrini, A., Lentz, S., Figueroa-Romero, C., Cerri, F., Backus, C., Hong, Y., Feldman, E.: Diabetes regulates mitochondrial biogenesis and fission in mouse neurons. Diabetologia 53(1), 160–169 (2010)
5. Knott, A.B., Bossy-Wetzel, E.: Impairing the mitochondrial fission and fusion balance: a new mechanism of neurodegeneration. Annals of the New York Academy of Sciences 1147(1), 283–292 (2008)
6. Lautenschläger, J., Prell, T., Ruhmer, J., Weidemann, L., Witte, O.W., Grosskreutz, J.: Overexpression of human mutated g93a sod1 changes dynamics of the er mitochondria calcium cycle specifically in mouse embryonic motor neurons. Experimental Neurology 247, 91–100 (2013)
7. Palmer, A.E., Giacomello, M., Kortemme, T., Hires, S.A., Lev-Ram, V., Baker, D., Tsien, R.Y.: Ca2+ indicators based on computationally redesigned calmodulin-peptide pairs. Chemistry & Biology 13(5), 521–530 (2006)
8. Rodner, E., Süße, H., Ortmann, W., Denzler, J.: Difference of boxes filters revisited: Shadow suppression and efficient character segmentation. In: Document Analysis Systems. pp. 263–269 (2008)
9. Süße, H., Ortmann, W., Lautenschläger, C., Körner, M., Schmidt, C., Stallmach, A., Denzler, J.: Oriented differences of boxes operators for blood vessel segmentation and analysis in confocal laser endomicroscopy images with minimal user interaction. In: Medical Image Understanding and Analysis (2013), 164–169
10. Westermann, B.: Mitochondrial fusion and fission in cell life and death. Nature reviews Molecular cell biology 11(12), 872–884 (2010)